Acta Materialia 133 (2017) 427–439

Contents lists available at ScienceDirect

Acta Materialia

journal homepage: www.elsevier.com/locate/actamat

Full length article

On the origin of primary ½ a_0 <111> and a_0 <100> loops in irradiated Fe(Cr) alloys

R. Schäublin [a, b, *], B. Décamps [c], A. Prokhodtseva [d, 1], J.F. Löffler [a]

[a] Laboratory of Metal Physics and Technology, Department of Materials, ETH Zurich, 8093 Zurich, Switzerland
[b] Scientific Center for Optical and Electron Microscopy, ETH Zurich, 8093 Zurich, Switzerland
[c] Centre de Sciences Nucléaires et de Sciences de la Matière (CSNSM), CNRS-IN2P3-Univ. Paris-Sud 11, UMR 8609, Bât. 108, 91405 Orsay, France
[d] Ecole Polytechnique Fédérale de Lausanne (EPFL), Centre de Recherches en Physique des Plasmas, Association Euratom-Confédération Suisse, 5232 Villigen PSI, Switzerland

ARTICLE INFO

Article history:
Received 8 October 2016
Received in revised form
10 January 2017
Accepted 13 February 2017
Available online 20 February 2017

Keywords:
Ultra-high purity Fe and Fe(Cr)
Transmission electron microscopy
Radiation damage
Dislocation loops
Materials for future fusion reactor

ABSTRACT

The radiation-induced primary dislocation loops in thin foils of ultra-high purity Fe and Fe(Cr) model alloys were investigated using ion irradiation in situ in a TEM. In the '111 mechanism' the induced nanometric loops of type a_0 <100> stem from mutual interaction of ½ a_0 <111> loops following their thermal diffusion. In the present work the conditions for this mechanism to occur are scrutinized. The effect of He, irradiation dose, dose rate, temperature and Cr content on the production of loops is assessed. Fe, Fe-5, -10 and -14Cr were irradiated with 500 keV Fe^+ and 10 keV He^+ ions up to 1 dpa and 1000 appm He at room and liquid nitrogen temperature. The initial loop population consists of ½ a_0 <111> and a_0 <100> loops, with no visible ½ a_0 <110>'s. Helium appears to stabilize ½ a_0 <111>'s by impeding their motion, as in its presence they are more numerous relative to a_0 <100>'s. At 1 dpa Cr plays a similar role. This is supported by (i) irradiations of Fe at three different dose rates, as only ½ a_0 <111>'s are observed after the fastest irradiation, and (ii) irradiation at liquid nitrogen temperature. The later leads to a majority of ½ a_0 <111>'s, while upon warming up to RT a_0 <100>'s become more numerous. All this supports the idea of the '111 mechanism'. However, surprisingly, at 0.05 dpa Cr actually favours the formation of a_0 <100> loops, irrespective of its influence on the mobility of the ½ a_0 <111>'s.

1. Introduction

Understanding the radiation damage mechanisms in ferritic-martensitic steels envisioned as structural material for future fusion reactors is crucial for their reliable and safe performance under the expected intense flux of 14 MeV fusion neutrons. Irradiation of metals with energetic particles leads to the formation of displacement cascades that engage tens of thousands of atoms to temperatures of thousands of Kelvin but during a very short time. The cascade is cooled down in few picoseconds at most, leaving a material fully recrystallized apart from a few point defects (self-interstitial atoms (SIAs) and vacancies) that may cluster into planar dislocation loops and voids. These irradiation-induced structural defects and transmutation-induced impurities such as H and He severely degrade mechanical properties of steels [1,2]. Ion irradiation of thin foils of materials with subsequent characterization by transmission electron microscopy of the defects produced is an efficient, flexible and fast way to study the primary radiation damage, especially in view of the availability of modern irradiation facilities allowing simultaneous dual and triple beam irradiation and in situ irradiation in transmission electron microscopy (TEM), such as the JANNuS facility in France [3].

In this paper we focus on the primary interstitial dislocation loops in Fe(Cr) (the basis of ferritic steels) for they constitute the majority of point defects clusters visible in the TEM. SIAs in bcc Fe are, according to ab initio simulations from the early 2000s [4,5], <110> dumbbells, which confirmed the idea based on experimental findings of the 1980s [6] using X-ray diffraction [7]. Simulations indicated that they can then cluster in parallel SIA agglomerates, namely dislocation loops [8,9]. However, such ½ a_0 <110> loops

* Corresponding author. Laboratory of Metal Physics and Technology, Department of Materials, ETH Zurich, 8093 Zurich, Switzerland.
E-mail address: rschaeublin@gmail.com (R. Schäublin).
[1] Present address: FEI Czech Republic s.r.o., Vlastimila Pecha 12, 627 00 Brno, Czechia.

http://dx.doi.org/10.1016/j.actamat.2017.02.041
1359-6454/

were never observed experimentally. Beyond a size of 5 SIA, i.e. about 0.5 nm in diameter, such a ½ a_0 <110> loop would transform into a ½ a_0 <111> loop [8], because the latter is the lowest in formation energy and the stacking fault energy in the {110} habit plane of the ½ a_0 <110> loop makes it energetically highly unfavorable. <110> SIA clusters were found by simulation to also occur as non-parallel SIA agglomerates in 2008 [10] such as the C15 configuration revealed in 2012 [11], but to this date none of these have been confirmed experimentally. Note that the C15 clusters would constitute 5% of the clusters produced by a displacement cascade [11]. The ½ a_0 <111> loops were observed in TEM in situ electron irradiation at room temperature of Fe thin foils in 1971 [12]. While the a_0 <100> loops in bcc Fe are energetically unfavorable at temperatures below 350 °C, according to elastic calculations [13] they occur at higher temperatures. As early as 1963 a case was reported where, in an Fe thin foil irradiated with ions at 550 °C, only a_0 <100> loops were observed in TEM [14]. In 1965 Masters postulated [15] that an a_0 <100> loop can stem from a reaction between ½ a_0 <111> loops, according to the reaction ½ a_0 [111] + ½ a_0 [$1\bar{1}\bar{1}$] → a_0 [100], the so-called '111 mechanism'. The a_0 <100> loops were observed following electron irradiation of Fe at 550 °C [16]; they were more recently reported for ion irradiations of UHP Fe and Fe(Cr) to 1 dpa at 500 °C [17,18]. It is thus usually considered, in agreement with literature results, that only ½ a_0 <111> and a_0 <100> type interstitial dislocation loops form in ferritic materials (for the sake of simplicity these are also called 111 loops and 100 loops, respectively). At 300 °C in Fe after 10 dpa irradiation only ½ a_0 <111> loops were observed [19], but other studies indicate that a_0 <100> loops are also present at 300 °C [20] or even dominate the loop population at 80% [21]; in this case Fe was neutron-irradiated to 0.06 dpa at 280 °C. The dislocation mechanism also depends on the loop size: in Fe at small sizes (few nanometers) a Burgers vector of ½ a_0 <111> and occasionally a_0 <100> is reported [22]. At larger sizes, beyond about 5 nm, dislocation loops can present both ½ a_0 <111> and a_0 <100> Burgers vectors [26,27]. Besides temperature and loop size, irradiation dose may be a key parameter. In ferritic materials, including steels, the situation is mixed (see e.g. Ref. [2]).

In our previous study [23,24] we irradiated ultra-high purity Fe and Fe(Cr) alloys with Fe ions in situ in a TEM with and without He to 0.5 and 1 dpa and up to 1000 appm He at room temperature in order to understand the primary dislocation loops occurring in these materials. It was concluded that the primary loop population consists of mobile dislocation loops of type ½ a_0 <111>. We concluded that the a_0 <100> loops can stem from the mutual interaction of the glissile ½ a_0 <111>'s according to the 111 mechanism.

In order to clarify the conditions for this mechanism to occur, we undertook the experimental study of radiation-induced nanometric dislocation loops in ultra-high purity Fe and Fe(Cr) alloys with respect to irradiation dose, dose rate, temperature (namely room temperature and LN2) and Cr content. The threshold dose for the first damage observable in TEM was investigated. The dislocation loop population in particular was quantified in terms of the number densities of loops per Burgers vector, either ½ a_0 <111> or a_0 <100>, and their ratio. For this purpose advanced TEM using convergent weak beam [25] and the new statistical **g**·**b** analysis method presented in Ref. [23] were applied to extract all possible microstructural information on the loops using diffraction contrast. The effect of the different parameters on the resulting microstructure and in particular on the formation of the ½ a_0 <111> and a_0 <100> loops is discussed.

Table 1
Compositions of the UHP materials investigated, in ppm unless otherwise stated.

Alloy	Cr	C	O	S	P
UHP Fe	<2 ppm	3	5	2	<5
UHP Fe-5Cr	5.40 wt%	3	4	3	<5
UHP Fe-10Cr	10.10 wt%	4	3	6	<5
UHP Fe-14Cr	14.25 wt%	4	4	6	<10

2. Experimental methods

Ultra-high purity Fe and Fe -5, -10, -14Cr alloys, designed by European Fusion Development Agreement (EFDA, now 'EUROfusion'), were specially fabricated at Ecole des Mines de Saint-Etienne for modelling-oriented irradiation experiments. The total concentration of the impurities did not exceed 30 ppm for all materials (Table 1). TEM sample foils were mechanically polished to a thickness of 50–100 μm. They were then thinned to electron transparency by electropolishing at 253 K using a solution of 11% perchloric acid in ethanol with 2% of butoxyethanol. The polished samples were first rinsed once in 233 K ethanol and then twice in RT ethanol. Further details are given elsewhere [23,24]. The determination of the Burgers vector **b** of the dislocation loops was made in TEM with the operating diffraction **g** applying an improved **g·b** analysis method using mainly weak beam dark field imaging mode, as detailed later. Note that in this paper micrographs are always presented in inverted contrast to improve the visibility of contrasts.

Irradiations in thin foils were performed at the JANNuS facility in Orsay, France (http://emir.in2p3.fr [3]). There, two ion accelerators are coupled to an FEI Tecnai G^2 200 kV TEM, impinging at a glancing 22° into the electron-transparent specimen areas. This allows irradiation with two ion beams simultaneously. During irradiation the microstructure was recorded using a GATAN ES500W Erlangshen CCD camera. During dual-beam irradiation it is not possible to simultaneously observe it with the electrons because the 10 keV He ions would be deflected by the TEM objective lens; the latter is thus turned off during irradiation. The materials investigated were irradiated at room temperature (RT) and liquid nitrogen temperature (LN2) with 500 kV Fe^+ together with or without 10 kV He^+ ions. The energy of the Fe^+ ions was chosen in such a way that the produced damage is maximal within the typical thickness of a TEM thin foil of about 100 nm. Likewise, the energy of He ions was selected in order to deposit them in the same region. Damage and He implantation profiles calculated with SRIM software are shown in Fig. 1.

Irradiations were performed under three different conditions:

(1) The first was a low-dose experiment, to 0.05 dpa with and without 50 appm He concentration, i.e. in single and dual-beam condition. These experiments complement the results of the single and dual-beam irradiations of the same materials to 1 dpa and 1000 appm He content reported earlier [23].
(2) The second was a dose-rate experiment, with UHP Fe irradiated at RT with single and dual-beam to 1 dpa without and with 1000 appm He concentration respectively, at three different dose rates, i.e. 0.55×10^{-4}, 2.50×10^{-4} and 5.50×10^{-4} dpa s^{-1}. They were optimized in order to get an observable degree of damage while limiting irradiation time to an acceptable range. In this way, for the lowest and highest dose rate irradiation, 1 dpa was achieved in 300 min and 30 min, respectively.
(3) The third was a low-temperature experiment to investigate the effect of temperature on the character of damage in UHP Fe irradiated in single beam to 1 dpa at liquid nitrogen temperature. Analysis of the produced defects was

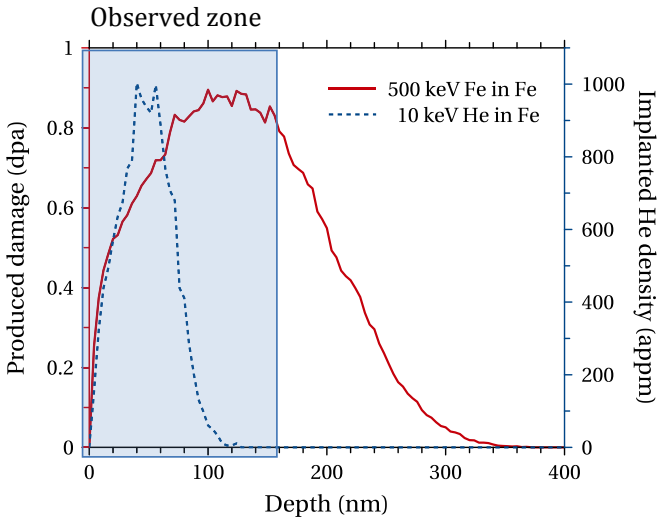

Figure 1. Simulated profiles of the 10 keV He^+ ion implantation (blue, right scale) and 500 keV Fe^+ induced displacement damage (red, left scale) in Fe (blue region: typical TEM thin foil) (SRIM simulation). (For interpretation of the references to colour in this figure legend, the reader is referred to the web version of this article.)

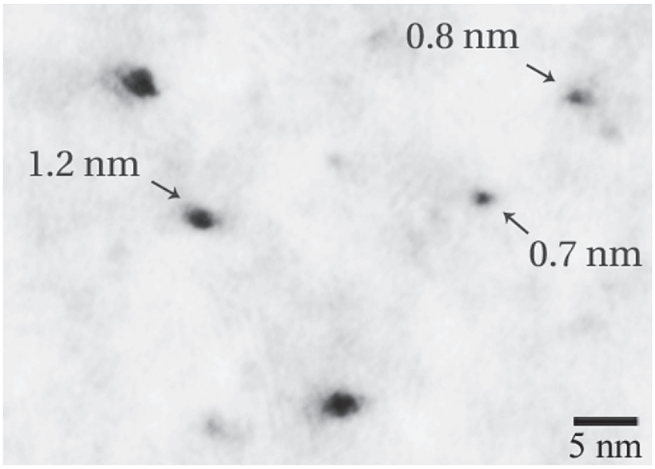

Figure 2. TEM CWBT **g** = {110} **g**(4**g**) micrograph, shown in inverted contrast, of a FIB lamella extracted from bulk UHP Fe irradiated in dual beam to 1 dpa and 1000 appm He at RT. Defects with sizes below 1 nm are resolved, provided the background intensity of the sample does not interfere with the observed defects. Objective aperture diameter is ~4 nm^{-1}. Micrograph made of 10 beam incidences taken within ~5 mrad in a single acquisition on photograph negative; total exposure time: ~10 s.

performed at low temperature and then at RT after warming. Details of the irradiation are given in Table 2.

Thickness of the regions of interest was measured in the TEM using electron energy loss spectrometry [26]. Note that for all TEM analyses we considered thicknesses from about 50 nm to 80 nm, because in thinner areas the proximity of the free surfaces strongly influence the radiation-induced microstructure [20] due to image forces [27], with a significant effect of the specimen crystal orientation on the defect yield [28]. In thicker areas the inelastic electrons blur the weak beam image [29]. The preliminary loops' Burgers vector established by **g**·**b** analysis was obtained in situ after single-beam irradiations. For the dual-beam irradiations, samples were exclusively investigated at the Paul Scherrer Institute, Villigen on a TEM JEOL JEM-2010 operated at 200 kV and equipped with a LaB_6 electron emitter. There the convergent weak-beam technique (CWBT) [25] was applied for all post mortem analyses. This method allows for higher precision in the analysis because of the smearing of the thickness oscillations: defects at all depths within the foil are revealed [23]. Note that defect sizes down to ~0.7 nm are measured reliably, which is about the diffraction limit (Fig. 2). A TEM FEI F20 at ScopeM ETHZ equipped with a field-emission gun and operated at 200 kV was used for standard checks.

Defects are considered to be dislocation loops with a Burgers vector ½ a_0 <111> or a_0 <100>, classic for bcc Fe. The case of ½ a_0 <110> will be treated later. Note that in this work loops do not exceed 10 nm in size. It is thus practically impossible to trace a single loop from one micrograph to another one recorded at a different diffraction condition. Therefore, a new method was applied in addition to CWBT: the statistical Burgers vector analysis [23], to obtain the absolute number density of defects per Burgers vector type. It consists of acquiring a series of n weak beam micrographs with n different diffraction vectors **g** and counting in each of them all visible loops, typically 100 to 500, to deduce their number density (in m^{-3}). The number density is given by the number of visible loops divided by the observed area volume, which is equal to the product of the observed area surface and its thickness. The defect densities are then considered in an overdetermined system of n equations (one per diffraction vector) that is solved using the least square method to obtain the absolute number density of defects, achieved here in MatLab®. The error of the result is given by the residuals of the least squares method. Further details on the statistical Burgers vector analysis method are

Table 2
Irradiation conditions (greyed-out conditions: irradiations reported in Ref. [23]).

Temperature	Material	500 keV Fe^+		10 keV He^+		Irradiation time [min]
		Dose [ions cm^{-2}] [dpa]	Fe flux [ions cm^{-2} s^{-1}] [dpa s^{-1}]	He content [ions cm^{-2}] [appm]	He flux [ions cm^{-2} s^{-1}] [appm s^{-1}]	
RT	Fe	1.0×10^{13}	1.2×10^{10}	4.25×10^{13}	5.5×10^{-5} dpa s^{-1}	15
	Fe-5Cr	0.05 dpa	5.9×10^{-5}	50 appm	0.055 appm s^{-1}	
	Fe-10Cr	9.5×10^{13}	2.8×10^{10}	6.7×10^{14}–7.5×10^{14}	2.8×10^{-4} dpa s^{-1}	56
	Fe-14Cr	0.45 dpa	1.3×10^{-4}	790–880 appm	2.8×10^{-1} appm s^{-1}	
		2.0×10^{14}	5.0×10^{10}	8.5×10^{14}	2.8×10^{-4} dpa s^{-1}	67
		1 dpa	2.5×10^{-4}	1000 appm	2.8×10^{-1} appm s^{-1}	
RT	Fe	2.13×10^{14}	1.2×10^{11}	8.5×10^{14}	5.5×10^{-4} dpa s^{-1}	30
		1 dpa	5.6×10^{-4}	1000 appm	5.5×10^{-1} appm s^{-1}	
			5.0×10^{10}		2.8×10^{-4} dpa s^{-1}	67
			2.5×10^{-4}		2.8×10^{-1} appm s^{-1}	
			1.2×10^{10}		5.5×10^{-5} dpa s^{-1}	300
			5.6×10^{-5}		5.5×10^{-2} appm s^{-1}	
LN2	Fe	2.2×10^{14}	1.2×10^{11}			30
		1 dpa	5.6×10^{-4}			

given in Ref. [23]. The output of the method is the absolute number density of loops with either ½ a_0 <111> or a_0 <100> Burgers vectors. The precision of the method is limited by (1) the number of visible loops (it has to be large enough to be statistically significant, typically more than few hundreds) and (2) by the visibility of the loops (besides the invisibility criterion given by $\mathbf{g}\cdot\mathbf{b} = 0$). Indeed, loops smaller than the diffraction limit have a contrast size remaining at the diffraction limit size, here about 0.7 nm (Fig. 2), but more importantly the contrast amplitude decreases with decreasing size to a level that can be below the noise level of the micrograph, thus rendering the smallest loops invisible (even if $\mathbf{g}\cdot\mathbf{b}\neq 0$). It is thus important to note that in this study only the defects that can be visible are considered, which excludes loops smaller than about 0.7 nm.

3. Results

3.1. Damage threshold and evolution of defect density during single-beam irradiation

Direct dynamic observations of the evolution of the radiation-induced microstructure were performed during single-ion beam irradiation. In this way it was possible to determine the threshold dose at which the first visible defects appear, as well as the density of produced defects as a function of the acquired dose. Note that invisibility of defects due to $\mathbf{g}\cdot\mathbf{b} = 0$ is not taken into account here, as it is not possible to perform the full analysis during the course of the irradiation. Typical sizes of the observed loops range from about 1 nm to a maximum of 7–8 nm in diameter.

During the irradiations to 0.45 and 1 dpa, which were performed at a higher dose rate, visible defects already appear several seconds after the start of irradiation. The damage threshold was thus estimated to be about 0.02 dpa, regardless of the material or crystallographic orientation of the foil [23]. Irradiations to 0.05 dpa were performed at a slower rate, thus allowing us to determine the threshold dose for the formation of visible defects with significantly greater precision. Fig. 3 shows the evolution of the microstructure as a function of the dose for the Fe-14Cr alloy: the first defects become visible at about 10^{-3} dpa or just below, as observed in UHP Fe, Fe-5Cr, Fe-10Cr and Fe-14Cr (Fig. 3(a)). Note that at this dose there is no overlap of the individual displacement cascades, which implies that we can see the residue of individual cascades in iron, and that this residue consists of dislocation loops as we will see later. The number of defects then increases linearly with dose (Fig. 3(c)).

3.2. Single and dual-beam irradiations to 0.05 dpa

3.2.1. Defect number density

Figs. 4 and 5 display the microstructure of UHP Fe, Fe -5, -10, -14Cr irradiated at room temperature to 0.05 dpa with 500 keV Fe^+ ions (left-hand column) or simultaneously implanted with 10 keV He^+ (right-hand column). Images are recorded using CWBT in regions with thicknesses of 50–80 nm. Considering the number of dislocation loops present, their nanometric size and the possible Burgers vectors, a classical $\mathbf{g}\cdot\mathbf{b}$ analysis is not tractable as described in part 2. For all materials irradiated both with single and dual-ion beams, clearly more defects are present in the images taken with $\mathbf{g} = \{200\}$, the difference being more notable in Fe-5Cr irradiated with a single beam (Figs. 3c and 4c). This observation points to the type of the Burgers vector of visible defects, because when imaged with $\mathbf{g} = \{200\}$ all four families of the ½ a_0 <111> type defects are visible, contrary to $\mathbf{g} = \{110\}$, where only half of the ½ a_0 <111> population can be seen. In order to quantify the damage produced in terms of fractions of defects with ½ a_0 <111> and a_0 <100> Burgers vectors, a detailed statistical analysis is crucial, as the apparent density of defects in the same sample differs significantly from one diffraction condition to another.

Fig. 4 shows TEM micrographs recorded with $\mathbf{g}$ vectors of {200} and {110} type of UHP Fe, Fe -5, -10, -14Cr irradiated to 0.05 dpa with 500 keV Fe^+ ions (left-hand column) or simultaneously implanted with 10 keV He^+ (right-hand column).

The presence of Cr or He does not seem to visibly affect the character of the damage produced. Only Fe-5Cr irradiated with both single and dual beams (Fig. 4c and d) and Fe-14Cr irradiated with dual beam (Fig. 4(h)) stands out, with a somewhat higher density of defects. However, at such a low dose the visible black dots are rather small, approaching the resolution limit of about 1 nm. Thus, careful investigation of every sample is required to reveal a general trend in the character of radiation-induced damage. The statistical $\mathbf{g}\cdot\mathbf{b}$ analysis method was applied, giving the total number density of defects as the sum of ½ a_0 <111> and a_0 <100> Burgers vectors. The results are presented in Fig. 5 together with the crystallographic orientation of the region where they were measured.

Fig. 5 reveals that the total density of visible defects produced in all materials after single-beam irradiation is significantly higher than after dual-beam irradiation, except for Fe-14Cr, where total densities are almost equal. In the single-beam case the highest total number density of defects was measured in UHP Fe. In addition, with increasing Cr content the total density decreases linearly. In

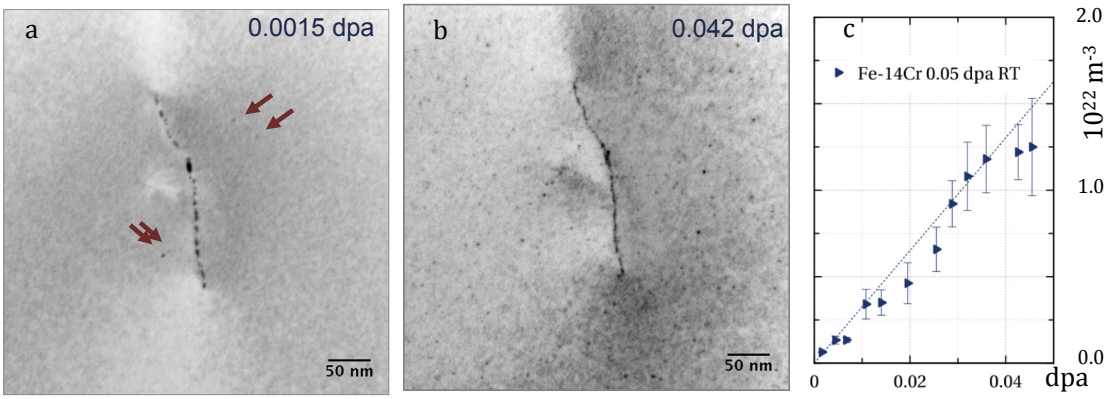

Figure 3. (a, b) Sequence of WBDF TEM micrographs of UHP Fe-14Cr recorded during irradiation with a single 500 keV Fe^+ ion beam to 0.05 dpa at room temperature, shown in inverted contrast. Diffraction vector $\mathbf{g} = \{110\}$, <100> zone axis, $\mathbf{g}(5\mathbf{g})$ weak-beam condition. First visible defects (indicated with arrows) appear at a dose of about 10^{-3} dpa. (c) Number density of visible defects as a function of dose.

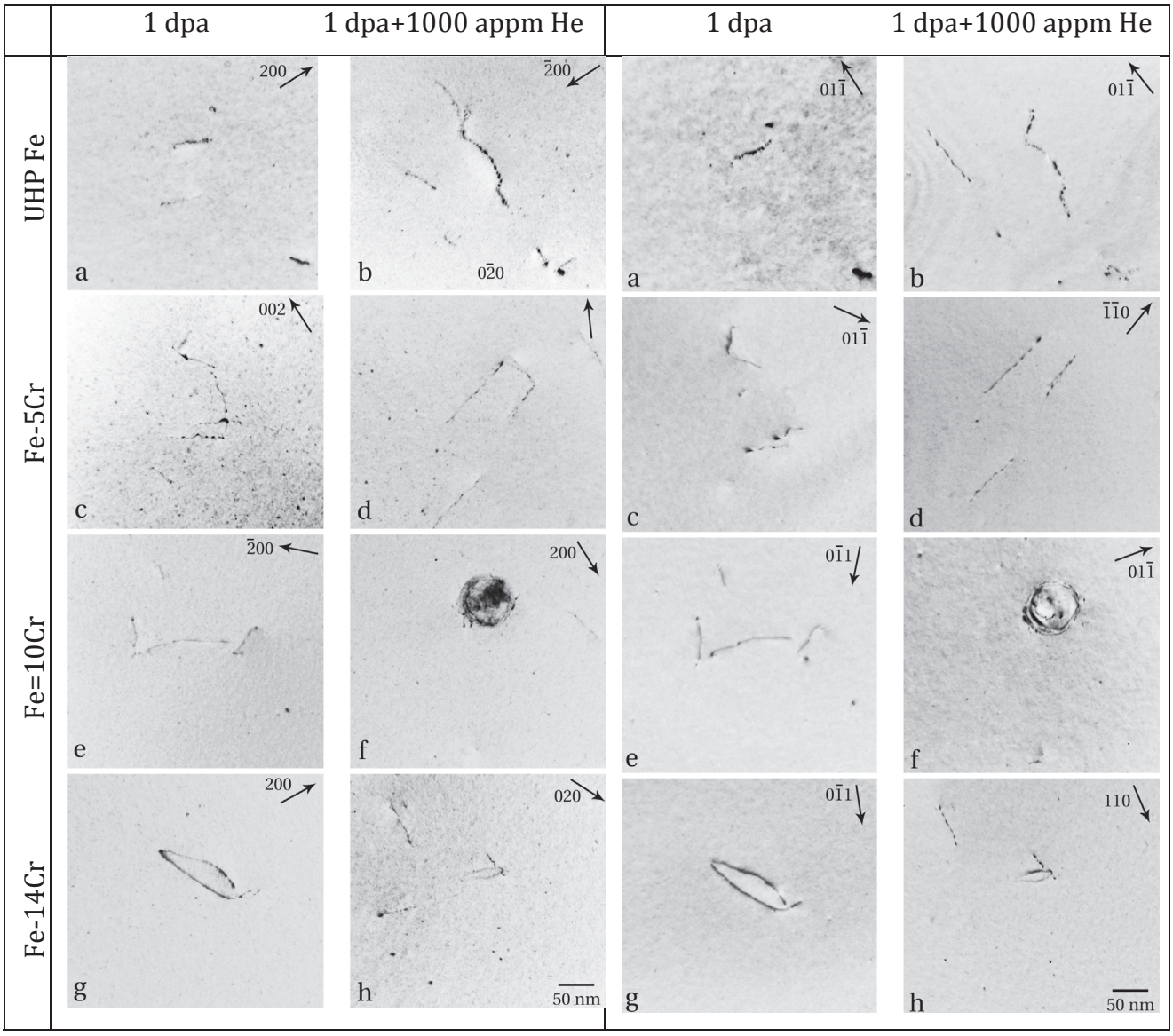

Figure 4. Sample of (a) UHP Fe, 70 nm thick; (c) Fe-5Cr, 70 nm thick; (e) Fe-10Cr, 55 nm thick; (g) Fe-14Cr, 70 nm thick, irradiated to 0.05 dpa at RT with 500 keV Fe^+. Sample of (b) UHP Fe, 80 nm thick; (d) Fe-5Cr, 80 nm thick; (f) Fe-10Cr, 80 nm thick; (h) Fe-14Cr, 70 nm thick, irradiated at RT to 1 dpa with 500 keV Fe^+ and implanted with 1000 appm He using 10 keV He^+. CWBT, $\mathbf{g} = \{200\}$, $\mathbf{g}(3\mathbf{g})$ and $\mathbf{g} = \{110\}$, $\mathbf{g}(4\mathbf{g})$ condition, 200 kV. Micrographs are shown in inverted contrast.

more detail, the total density of visible defects decreases from $10.6 \pm 1.4 \times 10^{22}$ m^{-3} for UHP Fe to $4.7 \pm 1.4 \times 10^{22}$ m^{-3} for Fe-14Cr. In Fe-10Cr irradiated in single-beam condition, several grains were available for investigations, among them [111] and [011] grains, and two grains with orientations between [011] and [001].

After dual-beam irradiation, of all materials UHP Fe shows the lowest total number density of visible defects, contrary to the single-beam case. Among the Fe(Cr) alloys the highest total density is measured for Fe-5Cr, while for Fe-10Cr the total density drops, though still exceeding that of UHP Fe. For Fe-14Cr it increases again. It thus appears that for Fe(Cr) alloys a minimum total defect density is observed for Fe-10Cr.

3.2.2. Defect size

Fig. 6 shows the size distributions of visible defects produced in the materials investigated under both single 500 keV Fe^+ and dual 500 keV Fe^+, 10 keV He^+ beam irradiations to the dose of 0.05 dpa and 50 appm He content.

In the Fe(Cr) alloys the diameter of almost all defects is between 0.5 and 1 nm; only a few loops larger than 2 nm are observed. The average size of visible defects does not depend on the Cr content or He presence. It is estimated to be 1.1 nm for all Fe(Cr) materials except for Fe-10Cr irradiated with dual beam, where the majority of defects are generally smaller, below 1 nm in diameter, with an average size of 0.9 nm. The sizes of defects produced in UHP Fe are slightly larger than in Fe(Cr): most are between 1 and 2 nm. However, again, the presence of He does not affect the size distribution; the average size of the defects after both single and dual-beam irradiations is about 1.4 nm.

3.2.3. Defect Burgers vector

The Burgers vector of the small dislocation loops was determined using the statistical method. It is assumed that the loops have a Burgers vector that is either ½ a_0 <111> or a_0 <100>. The resulting number densities of defects with ½ a_0 <111> and a_0 <100> Burgers vectors produced after the irradiation with single

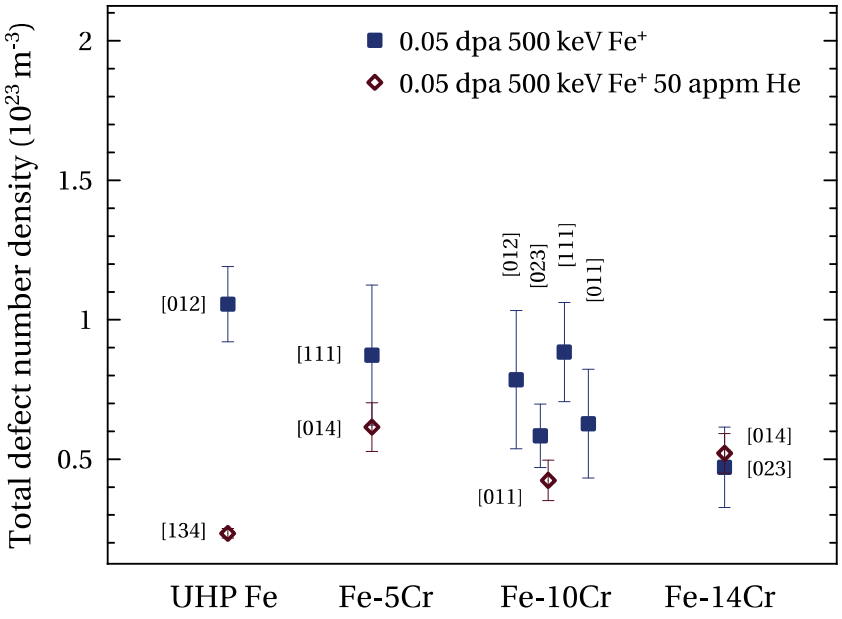

Figure 5. Total defect number density in UHP Fe, Fe-5, -10, -14Cr irradiated at room temperature to 0.05 dpa with or without 50 appm He, calculated with the statistical **g**·**b** technique with the indicated crystallographic orientation of the thin foils.

and dual beam are plotted in Fig. 7 and Fig. 8, respectively. The crystallographic orientation of the investigated region is indicated for each specimen.

After single-beam irradiation in UHP Fe and Fe(Cr) alloys the majority of resolved dislocation loops are of type ½ a_0 <111>, their fraction of total defects ranging from 60% for Fe-5Cr up to 100% for UHP Fe and [111] grain of Fe-10Cr. Only Fe-14Cr stands out, with the inverse balance of ½ a_0 <111> to a_0 <100> loops, namely 45% versus 55%. It appears that the number of defects with ½ a_0 <111> Burgers vector decreases with increasing Cr content, including UHP Fe in this trend. Dislocation loops with a_0 <100> Burgers vector are produced in lower amounts than those of type ½ a_0 <111>, and their density in general does not depend on chromium content.

In the dual-beam case in all materials investigated only loops with ½ a_0 <111> Burgers vector are found. There is no clear dependence of the number of ½ a_0 <111> loops and, hence, the total

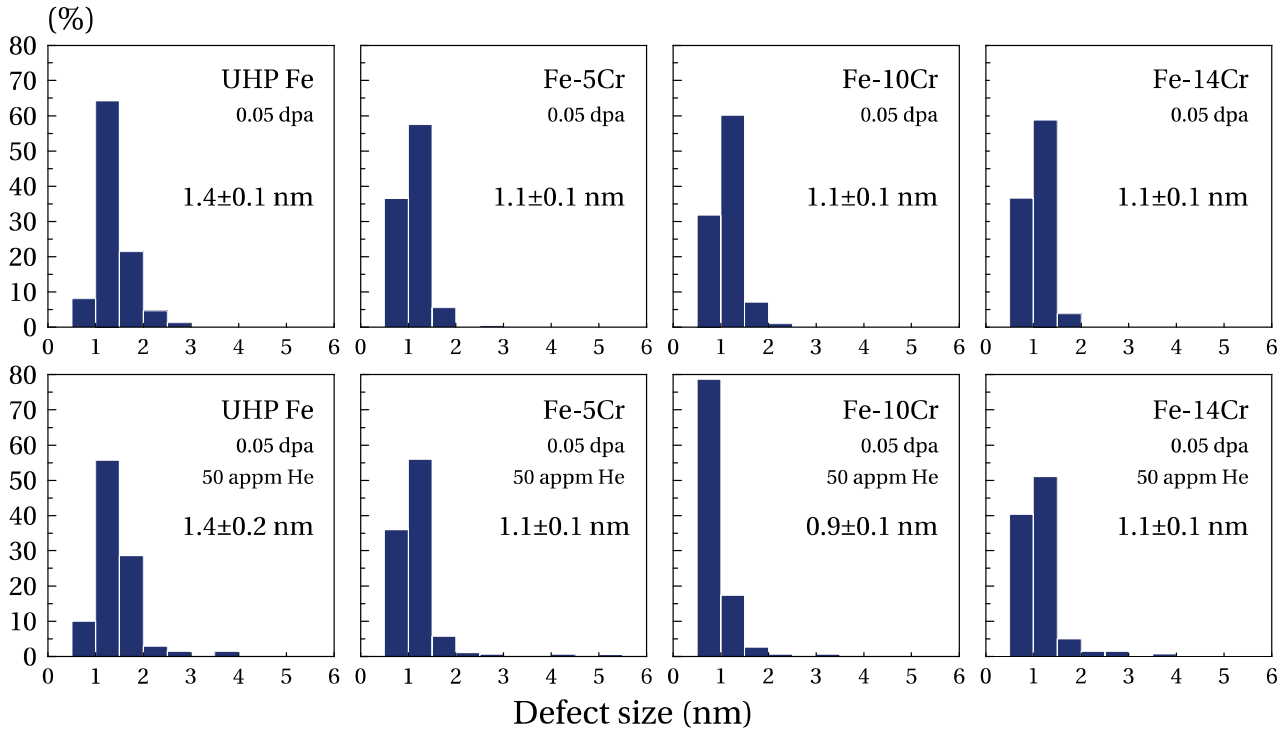

Figure 6. Distribution of TEM image size of defects produced in UHP Fe and UHP Fe-5, -10 and -14Cr alloys following 500 keV Fe^+ single-beam and 500 keV Fe^+, 10 keV He^+ dual-beam irradiations at room temperature to 0.05 dpa and 50 appm He. The respective average size is given in each distribution chart.

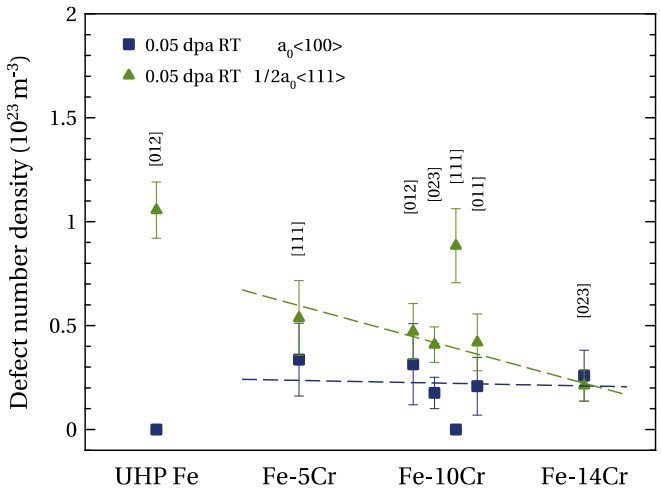

Figure 7. Density of defects with ½ a_0 <111> and a_0 <100> Burgers vectors in samples irradiated with single 500 keV Fe^+ ion beam to the dose of 0.05 dpa at RT. The foil normal is indicated for each region investigated. The error bar for values zero is a few 10^{21} m^{-3} and hidden by the data symbol.

number density of visible defects on the chromium content. The lowest density of defects is observed for UHP Fe, with Fe(Cr) alloys showing significantly a higher number density. Among Fe(Cr) materials, Fe-10Cr has a slightly lower defect density than Fe-5Cr and Fe-14Cr.

3.3. Effects of dose rate in UHP Fe

In order to investigate the effects of the dose rate of the incoming ions on the character of damage produced in single and dual-beam cases, UHP Fe was irradiated at three dose rates at room temperature with 500 keV Fe^+ ions to 1 dpa with and without 1000 appm of He implanted as 10 keV ions. High dose-rate single and dual-beam irradiations lasted 0.5 h at a rate of damage production of 5.5×10^{-4} dpa s^{-1} and 0.55 appm s^{-1} for the rate of He implantation. Low dose-rate irradiations were ten times slower, lasting 5 h, with corresponding irradiation/implantation rates of 5.5×10^{-5} dpa s^{-1} and 0.055 appm s^{-1} for Fe and He ions, respectively. Another set of irradiations was performed at a rate of 2.8×10^{-4} dpa s^{-1} and 0.28 appm s^{-1} for Fe and He ions, respectively, which is two times slower than for the highest dose-rate irradiations.

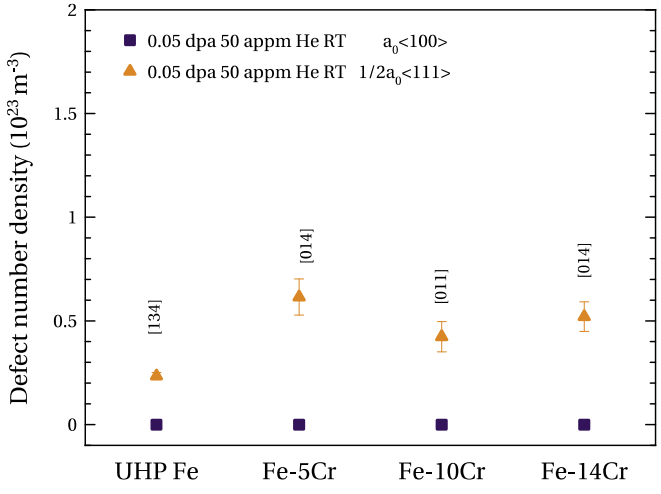

Figure 8. Density of defects with ½ a_0 <111> and a_0 <100> Burgers vectors in samples irradiated with dual 500 keV Fe^+ and 10 keV He^+ ion beam to the dose of 0.05 dpa and 50 appm He content at RT. The foil normal is indicated for each region investigated. The error bar for values zero is a few 10^{21} m^{-3} and hidden by the data symbol.

In the single-beam case direct observations of the defect evolution under irradiation were performed for the 5.5×10^{-4} dpa s^{-1} and 5.5×10^{-5} dpa s^{-1} dose rates. The density and size of defects are retrieved from the images recorded during irradiation. Fig. 9 presents the evolution of the density of visible defects with dose for different dose rates.

It appears that the number density of defects does not depend on the dose rate. For both the highest and lowest dose rate, density grows linearly up to about 0.3 dpa, beyond which saturation is reached. As for the average size, larger defects are clearly observed in the case of the lowest dose rate. For both dose rates defect size is generally not dependent on the dose; only slightly smaller defects are observed at the beginning of the irradiations, which implies that the average defect size follows the same trend as density, reaching saturation at about 0.3 dpa.

Irradiated thin foils were investigated post mortem. Results obtained using statistical Burgers vector analysis are presented in Fig. 10(a) and (b) with respect to dose and He implantation rate for dual-beam cases. The total density of visible defects is shown in Fig. 11. For the sake of clarity dose rate is plotted on a logarithmic scale.

Fig. 10(a) shows that after single-beam irradiation the density of both a_0 <100> and ½ a_0 <111> type defects is not affected by the dose rate. In general, loops with ½ a_0 <111> Burgers vector are found in slightly lower numbers than those with a_0 <100>. In more detail, the ratio of ½ a_0 <111> loops to a_0 <100> loops is estimated to be between 30 and 45% regardless of the dose rate, with only one exception, where it is more than 60%. However, it appears that the dose rate has a notable effect on the types of loop observed after dual-beam irradiation.

As shown in Fig. 10(b), at the highest dose rate the defect population is dominated by ½ a_0 <111> loops, 100% of visible defects being of this type. For the medium dose rate a relatively small number of a_0 <100> loops, about 15% of total population, is observed, and for the lowest dose rate the density of a_0 <100> and ½ a_0 <111> loops is similar. To sum up, the total density of visible defects in the single-beam case does not depend significantly on the dose rate. After dual-beam irradiation at the lowest dose there is a slight decrease in the total density of defects compared to the two highest dose rates, at which the total densities are identical, indicating a possible saturation of the dose-rate effect on the number density.

For thin foils irradiated with single and dual beam at the highest dose rate enough data were obtained to perform an extended statistical **g**·**b** analysis and thus distinguish between the dislocation loops belonging to four different families within the ½ a_0 <111> type Burgers vector: ½ a_0 [111], ½ a_0 [$\bar{1}$11], ½ a_0 [1$\bar{1}$1] and ½ a_0 [11$\bar{1}$]. It appears that in UHP Fe irradiated in single beam at high dose rate, 5.5×10^{-4} dpa s^{-1}, the proportion of families of type ½ a_0 <111> defects are distributed according to their orientation towards the free surface. The vector normal to the investigated grain in this case is [225]. In more detail, defects with Burgers vector ½ a_0 [111] and ½ a_0 [11$\bar{1}$] oriented at 19° and 51° towards the foil normal are not present at all and the sum of ½ a_0 [$\bar{1}$11] and ½ a_0 [1$\bar{1}$1] defects, which are oriented almost parallel to the surface of the sample, constitute the full 111 loop population.

Conversely, in UHP Fe irradiated at the same dose rate in presence of He, the ½ a_0 <111> families are equalized in the foil, supporting the idea that He stabilizes mobile ½ a_0 <111> loops. So, among a total of 100% of ½ a_0 <111> loops 22 ± 14% are ½ a_0 [111], 52 ± 9% are ½ a_0 [$\bar{1}$11] and ½ a_0 [1$\bar{1}$1] together and, finally, 26 ± 13%

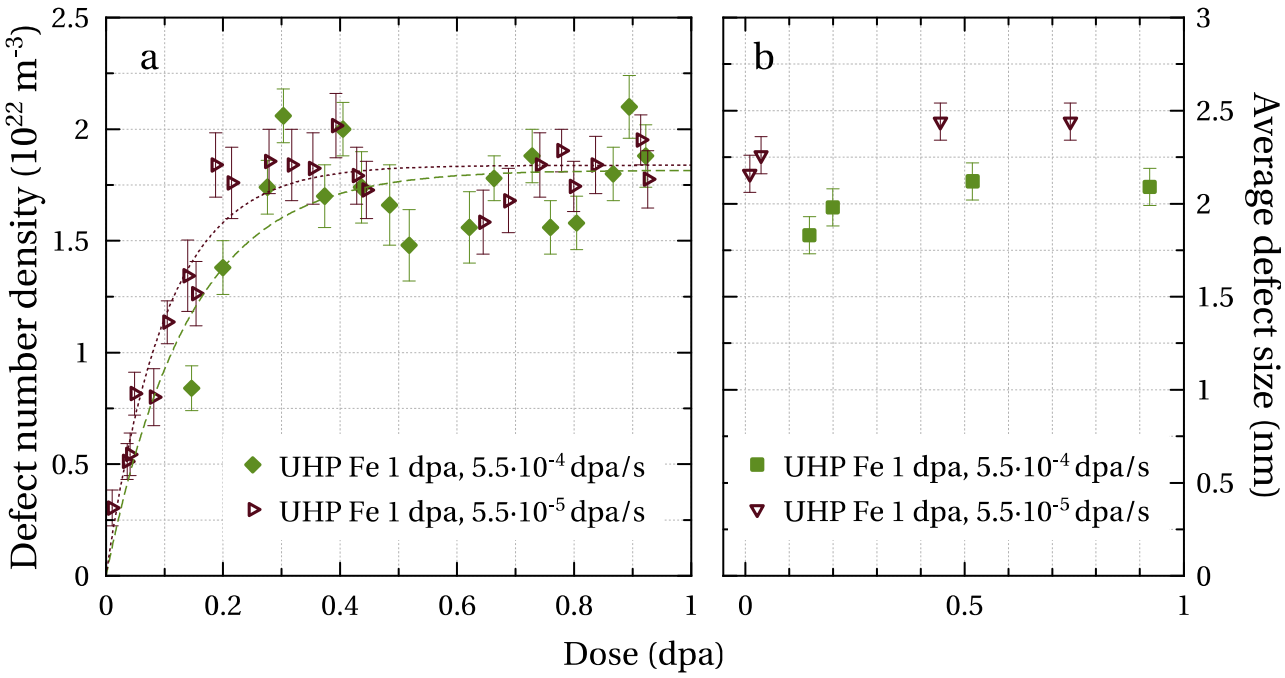

Figure 9. Evolution with dose of (a) the number density of visible defects and (b) the average defect size in UHP Fe irradiated to 1 dpa at 5.5×10^{-4} dpa s^{-1} and 5.5×10^{-5} dpa s^{-1} dose rates. Results are obtained from the TEM images recorded during irradiation with a diffraction vector $\mathbf{g} = \{110\}$, $\mathbf{g}(5\mathbf{g})$ weak-beam condition. Density is not corrected for invisibilities due to $\mathbf{g}\cdot\mathbf{b} = 0$.

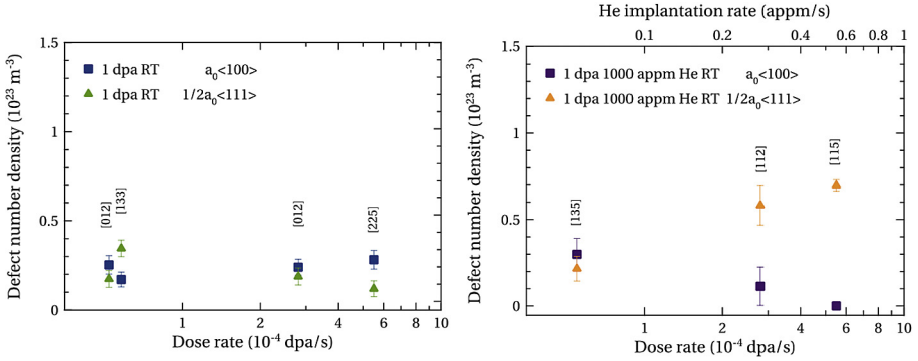

Figure 10. Density of defects with a_0 <100> and ½ a_0 <111> Burgers vectors in UHP Fe irradiated at RT with (a) single 500 keV Fe$^+$ ion beam at 5.5×10^{-5} dpa s^{-1}, 2.8×10^{-4} dpa s^{-1} and 5.5×10^{-4} dpa s^{-1} and (b) dual 500 keV Fe$^+$ and 10 keV He$^+$ ion beams with 0.55, 0.28 and 0.055 appm s^{-1} He implantation, respectively. The foil normal is indicated for each region investigated.

belong to the ½ a_0 [11$\bar{1}$] family. Normal to the foil in this case is [115], hence, the orientations of the families to it are 27°, 85°, 85° and 43°, respectively.

3.4. Effects of the irradiation temperature in UHP Fe

Irradiation at liquid nitrogen temperature allows studying the irradiation-induced microstructure with a reduced effect of thermal evolution, thus maximizing the chances of observing defects stemming directly from the displacement cascades. UHP Fe was irradiated with a single 500 keV Fe$^+$ ion beam to 1 dpa at 93 K, at a dose rate of 5.5×10^{-4} dpa s^{-1}. The irradiated thin foil was tilted to achieve several diffraction conditions in order to determine the Burgers vectors of the visible defects. The sample was then warmed to room temperature and transported to PSI Villigen, where the investigated region was traced back and analyzed in TEM.

Fig. 12a and b shows TEM pictures of approximately the same region of the irradiated sample recorded at low temperature and after warming to room temperature. Images were taken with a $\mathbf{g} = (011)$ diffraction vector close to the [011] zone axis. The thickness of the regions was about the same: 100 nm measured from the number of thickness fringes for Fig. 12(a), and 130 nm measured from the EELS spectrum for Fig. 12(b). It is seen that the density of visible defects is higher at low temperature, which appears logical, as the mobility of the defects is reduced and, hence, fewer defects are being eliminated to free surfaces or by annihilation. Detailed statistical Burgers vector analysis reveals that the total density of defects produced drops from 9.8 (±0.1) × 10^{22} m^{-3} at 93 K to 5.8 (±0.5) × 10^{22} m^{-3} at room temperature. The decrease happens at the expense of ½ a_0 <111> loops, whose absolute density diminishes more than two-fold after warming, while the density of a_0 <100> loops remains approximately the same: 2.6 (±0.1) × 10^{22} m^{-3} and 3.0 (±0.4) × 10^{22} m^{-3} for 93 K and room temperature, respectively. In thinner areas loss of ½ a_0 <111> loops after warming to room temperature is even more pronounced. Indeed, in the 60 nm thick region, located near the previous ones, the density

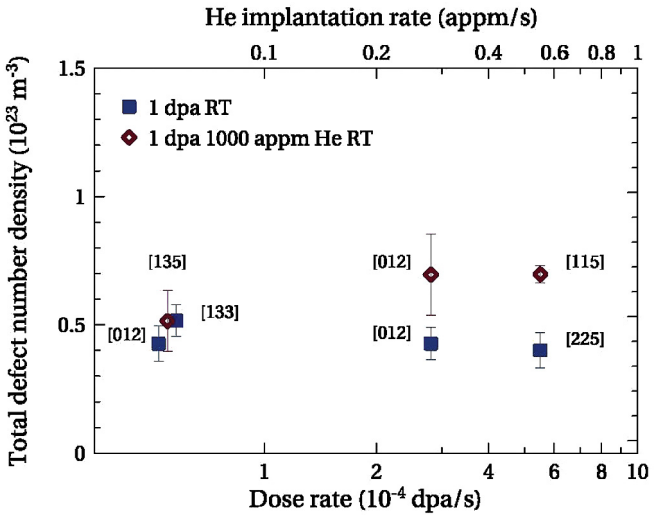

Figure 11. Total density of defects in UHP Fe irradiated at RT with single 500 keV Fe^+ and dual 500 keV Fe^+ and 10 keV He^+ as a function of dose rate. Dose rate is 5.5×10^{-5} dpa s^{-1}, 2.8×10^{-4} dpa s^{-1} and 5.5×10^{-4} dpa s^{-1} with or without He at a rate of 0.55, 0.28 and 0.055 appm s^{-1}, respectively. The foil normal is indicated for each region investigated.

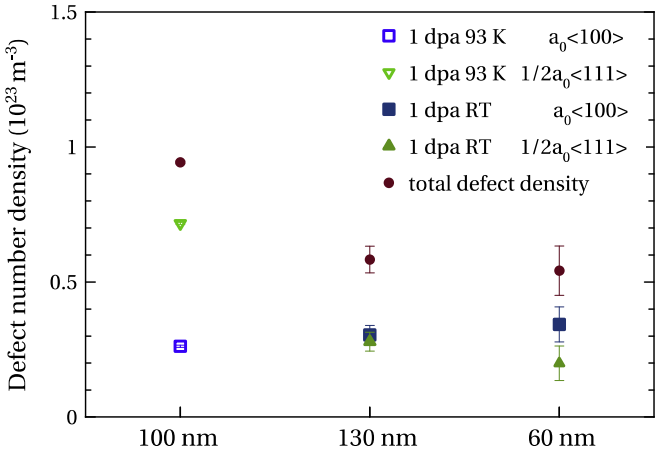

Figure 13. Density of ½ a_0 <111> and a_0 <100> loops and total density of dislocation loops in UHP Fe produced by irradiation to 1 dpa at 93 K and after warming to RT. At RT defect analysis was performed in two neighbouring regions of different thickness. The thickness of the investigated regions is shown in the graph. The foil normal is close to <110>.

of ½ a_0 <111> loops is 2.0 (±0.6) × 10^{22} m^{-3} and that of a_0 <100>'s is only slightly increased compared to the thicker regions, as seen in Fig. 13.

The relative proportion of ½ a_0 <111> loops decreases significantly after the sample is warmed, resulting in a population dominated by a_0 <100> loops whose density is slightly higher than the one at 93 K. The decrease of the number of ½ a_0 <111> loops can thus be due to their escape to the free surfaces and to their recombination in a_0 <100> loops through the 111 mechanism.

Another interesting result can be deduced from the **g**·**b** data recorded at low temperature: using extended statistical analyses of the Burgers vector it is possible to assess the presence or absence of ½ a_0 <110> defects postulated long ago and also to test the reliability of the statistical method. When one considers the ½ a_0 <110> loops in the statistical analysis, along with ½ a_0 <111> and a_0 <100> loops, the solution of the equation system shows that no ½ a_0 <110> loops are visible in the foil. However, according to simulations it is unlikely that faulted ½ a_0 <110> loops can grow to the sizes resolved in TEM. In this way, statistical Burgers vector analysis confirms that if ½ a_0 <110> defects are present, their size is below the resolution limit of the microscope, i.e. below about 1 nm.

4. Discussion

Before discussing the results, we will provide a focused summary of the knowledge on the primary damage. Displacement cascades in bcc Fe give rise to SIAs and vacancies. MD simulations of Fe cascades indicate that the fraction of clustered to individual SIAs is 50%, with many clusters in the form of glissile 111 interstitial loops [30]. No 100 interstitial loops by MD have been reported yet. The fraction of sessile to glissile SIA clusters in pure Fe is significant, at 30–50% [30]; however the sessile clusters (including the recently discovered C15 cluster [11]) have yet to be revealed experimentally, via (e.g.) TEM. According to MD and kinetic Monte Carlo of Fe, vacancies clusters are in lesser proportion than SIAs and their clusters are much smaller (<15 vacancies) [30,31]. Only two cases indicate the possible formation of vacancy dislocation loops directly from the displacement cascade: Soneda et al. [32] observed only one 100 vacancy loop in one hundred simulated cascades of 50 keV in Fe (many 111 interstitial loops were also always present). In the case of

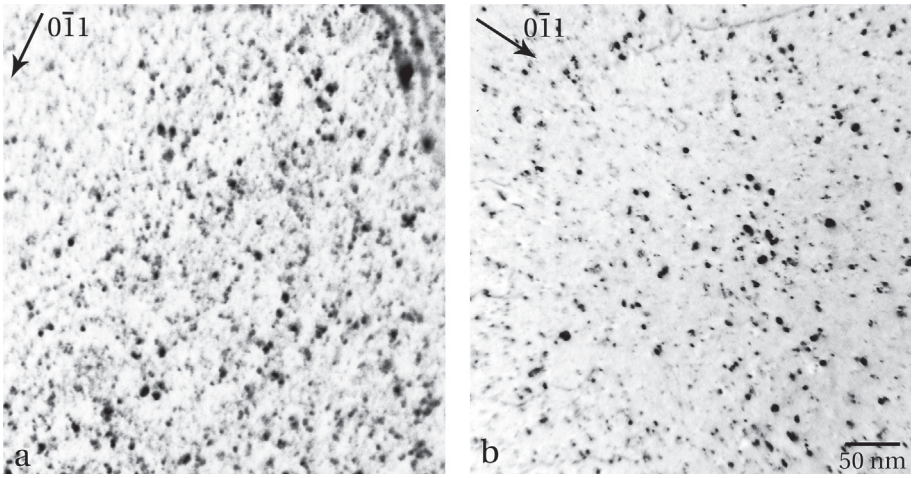

Figure 12. (a) WB **g** = (011) **g**(5**g**) micrograph recorded at 93 K of UHP Fe irradiated with 500 keV Fe^+ to 1 dpa at 93 K, (b) CWBT **g** = (011) **g**(4**g**) micrograph recorded after warming to room temperature. The regions in pictures (a) and (b) are not identical, but were recorded at nearby locations.

near-surface displacement cascades in Fe, recent simulations by different groups yielded various 100 vacancy loops and few 111 ones [33,34], revealing the strong impact of a free surface on the damage produced when located within about 10 nm from it. This is confirmed by experimental results in Fe [28]. It should be noted that MD simulation of the formation energy of various vacancy cluster configurations in Fe as a function of size indicates that the void is the most favourable one [35]. In sum, vacancies in bulk Fe (i.e. away from a free surface) either remain unclustered or cluster in sub-nanometric voids; it thus seems reasonable to consider in the following discussion that loops are interstitial in nature.

In Ref. [23] we saw that in pure Fe irradiated at RT with only Fe ions at 0.45 and 1 dpa there is a majority of 100 loops, and few 111 ones. This is also reported in Refs. [28,36] for a similar dose (1.6 dpa) at RT and 300 °C. These authors [28,37] noted that the defects density strongly depends on the crystal orientation, with a complete loss of defects in pure Fe for a <111> foil normal. This can be explained by the impact of the free surfaces, which increases with decreasing sample thickness, accompanied by a stronger dependence on the crystal orientation as mentioned in part 2. We have not observed such a dependence on crystal orientation in our study and in Ref. [23], presumably because our thicknesses (>50 nm) are larger than the one they used (around 30 nm), thus preventing a too strong effect of the free surfaces. At higher doses (6.5–10 dpa) at RT and in thicker areas (>60 nm) these authors report, in Ref. [20], the formation of strings of 111 loops. We note that this indicates that the spontaneous transformation from 111 loops to 100 loops as proposed in Ref. [38] is not occurring in this case. This can be due to the blocking of the 111 loops in the strings, frustrating the 111 mechanism. From these findings it was concluded that 111 loops constitute the primary damage, as also indicated by MD simulations [30], and that 100 loops come mainly from the interaction of the mobile 111 loops [23], according to the reaction $\frac{1}{2}\,a_0\,[111] + \frac{1}{2}\,a_0\,[1\bar{1}\bar{1}] \rightarrow a_0\,[100]$. This '111 mechanism' was first deduced from experimental observations in 1965 [15] and later explored by MD simulations [39], where a completed reaction was reported only recently [40]. We saw that in the presence of He the ratio of the 111 to 100 loops was reversed [23]. MD simulations indicate that He segregates to the 111 loops [41,42], and He stabilizes vacancy clusters (eventually forming He bubbles) [43,44]. Both mechanisms may impede 111 loops mobility, thus reducing their mutual interaction, which in turn frustates the formation of 100s. Note that the same idea was put forward recently to explain the higher number density and size of 100 loops in 500 °C dual-beam ion irradiation of the same materials [18]. According to this view the 111 loops thus dominate the microstructure in the presence of He. A similar trend was observed with Cr in single-beam irradiations [23]: in its presence the majority of the loops are 111, contrary to pure Fe. It was concluded that Cr in Fe also impedes the mobility of 111s [23]. MD simulation results confirm this behaviour for both small SIA clusters [45] and 111 loops [46]; it is due to Cr segregation to the loops [46]. In the presence of He and Cr the situation was less clear, but the expected result would be that with the two elements impeding the 111 motion much fewer 100 loops would be observed, which was not the case: there were still more 100 loops than in the case of pure Fe with He [23]. A synergistic effect of He and Cr was proposed. We will see in the following that the present results confirm that, firstly, the 111s constitute the primary loop population, and, secondly, that Cr actually favours the formation of 100 loops, irrespective of the fact that it may or may not influence the mobility of 111 loops.

The present experiment at the **low dose** of 0.05 dpa allowed us to explore the microstructure evolution when time is short (relative to the previous irradiation at 0.5 to 1 dpa reported in Ref. [23]) and thus to see what happens at the beginning of the irradiation-induced microstructure evolution. At this dose in pure Fe only 111 loops are visible, and no 100 loops (Fig. 7). In view of the 111 mechanism, the lack of 100s at 0.05 dpa may thus originate in the lack of interaction between 111s, because of (1) their much lower number density due to the dose (10 times lower) and (2) the reduced available time for their interaction because of the shorter irradiation. Their integrity is thus preserved and they dominate the microstructure. Thanks to the short available time the effect of the incorporation of He is now even clearer; in this case no 100 loops are visible, which confirms that (1) primary loops are 111s and that (2) their mobility is limited by He. Only their visible density is affected, with an apparent reduction, because the decrease in their diffusity due to He impedes their growth and thus their visualization in the TEM. When enough time is given (as reported in Ref. [23]) 111 loops can move more and thus interact to result in the formation of 100s. At low doses, in the case of the material containing Cr and in the single-beam case, curiously, while the majority of the loops are 111, many 100s are visible. It thus appears that **at low dose** and in the single-beam case, Cr actually favours the formation of 100 loops (see Fig. 7 of this paper), as they are not visible in pure Fe. In addition, dual-beam results confirm that the presence of He reduces the mobility of 111 because the formation of 100 is completely restricted in all cases, irrespective of the Cr content (Fig. 8).

At high dose [23], or when more time is for the 111 loop diffusion to occur, one expects to see more 100 loops due to their facilitated interaction. This is clearly so in the single-beam case in pure Fe (Fig. 11 in Ref. [23]), with the 100 character dominating the loop population. In Fe(Cr), one sees some 100 loops, but the 111s still constitute the majority, confirming the idea that Cr can impede the mobility of 111s [23]. In the dual-beam case, the presence of He hinders the formation of 100 loops because He impedes the movement of 111 loops. This is clearly seen in pure Fe, but with Cr it appears that 100 loops still form, and in quantities slightly larger than in pure Fe (Fig. 12 in Ref. [23]). In presence of Cr, He thus seems to be less capable of impeding the formation of 100s if enough time is given, which strengthens the intriguing idea that **Cr actually favours the formation of 100 loops**. This could be due to several atomistic mechanisms, of which three seem to fit the present results. Let us first consider the cases without He, where 100 loops are observed in presence of Cr.

(1) There may be a **catalytic effect** whereby the Cr atoms are the locations where the 111 loops experience a spontaneous reaction and transform to 100. This was proposed by Arakawa (but in pure Fe) on the basis of experimental observations [38]. This catalytic effect may also reveal itself in the result of the reaction between 111 loops, whereby 100 loops would be promoted by the presence of Cr; however, recent MD simulations [47] indicate that the impact of Cr on such a reaction is low, and if anything would cause the opposite effect and actually promote 111 loops.

(2) There may be an **acceleration effect** whereby Cr would actually favour the diffusion of the 111 loops, which in turn would favour the formation of the 100 loops. An accelerating effect was revealed by MD simulation in Fe(Cr) for the single SIAs mobility. It is increased in the presence of Cr, but only at temperatures below about 400 K; at higher temperature Cr reduces SIA diffusion [48]. However, the mobility of the SIA clusters in MD simulations appears to be consistently reduced by the presence of Cr, with a minimum at 10% Cr for small clusters. It shifts towards lower concentrations with

increasing cluster size [49]. To sum up, MD simulations do not support an acceleration effect on the mobility of SIA clusters due to Cr.

(3) There may be a **bias effect**, whereby due to the presence of Cr in the damage left by the displacement cascade after cooling, some 100 loops may form readily, in addition to the 111 loops. However, MD simulations show that displacement cascades in pure Fe mainly generate 111 loops [50], no 100 loops [51], and some 3D SIA sessile configurations [30]. It should be noted that the fraction of sessile to glissile SIA clusters in pure Fe is indeed significant, at 30–50% [30]; however, these have not yet been revealed in TEM. Note also that the fraction of clustered SIAs is 50% [30]. In Fe(Cr) Terentyev et al. [52] found by MD simulations that Cr in Fe does not seem to affect the damage resulting from cascades significantly, at least in terms of point defects number densities and clusters densities and sizes (there was no indication of the type of clusters). To sum up, at this point MD simulations do not support the bias hypothesis of the direct formation of 100s due to Cr in Fe displacement cascades.

In the presence of He the role of Cr is more complex. An MD study [53] showed that Cr reduces the mobility of He in Fe(Cr) relative to pure Fe, with consequently less He decorating the 111 loops. In this view, Cr may mitigate the impact of He: in the presence of Cr, the reduction in mobility of the 111 clusters by He would be less than in pure iron. This should in turn allow them to remain mobile and form 100 loops. This is the case for the high dose in the present study [23]. However, in the low-dose irradiation of the materials containing Cr the contrary is observed; when He is present no 100 loops are present, challenging this idea, but it should be noted that the time may be too short for any mechanism involving mobility to operate. There may be other synergistic effects between Cr and He on the damage resulting from displacement cascades, as indicated by recent MD studies [54]: interstitial He could increase the number of point defects. However at the content of interest here, 1000 appm He, the impact of He is insignificant [54]. In pure Fe we saw a similar situation, where He at these concentrations has an insignificant impact on the resulting point defects number [42]. To sum up, in MD simulations He has no effect on the formation of dislocation loops in displacement cascades. We therefore conclude that He only affects the mobility of the 111s.

The **dose rate** has an impact on the resulting irradiation-induced microstructure. In UHP Fe in the single-beam case the dose rate does not significantly affect either the total number density or the fraction of 111 to 100 loops. Conversely, in the dual-beam case and for the same dose the resulting number density of dislocation loops increases with an increasing dose rate. The fraction of 111 to 100 loops also increases strongly with increasing dose rate. These results can be analyzed in view of the 111 mechanism; in the case of the single-beam irradiation the 111 loops move freely and seem to have enough time to cover sufficient distances to interact and form a significant fraction of 100 loops at any of the dose rates investigated. We have seen that in some cases the 100 loops dominate the microstructure, with only few 111s. In the dual-beam case, however, i.e. in the presence of He, at the highest dose rate the 111 loops impeded by He do not have enough time to move and interact to form 100 loops, while at the lowest dose rate a significant fraction of 100 loops are again formed, indicating that here the 111 loops had time to move and interact. To sum up, the dose-rate experiment findings support the 111 mechanism.

The **temperature** also has a significant impact on the resulting microstructure, in particular on the fraction of 111 to 100 loops. In effect, at liquid nitrogen temperature in UHP Fe and upon single-beam irradiation the 111 loops dominate the microstructure over the 100s. This indicates that the 111 loops are immobilized by the low temperature. Upon heating to room temperature the ratio of 111 to 100 loops reaches about 1 and the density of 100 loops slightly increases. This indicates that the 111 loops have moved (1) to escape to the free surfaces and (2) to interact and form 100s because of the observed increase of their number density. In sum, the low-temperature experiment supports the idea that 111 loops are the source of 100 loops.

In summary, it appears that 111 loops constitute the primary loops and that the '111 mechanism' for the 100 loop formation satisfactorily explains the comparative results on the dislocation loop populations obtained at 1 dpa and at RT in single and dual-beam experiments in pure Fe and in Fe(Cr). The key mechanism is the mobility of the 111 loops, which is reduced by He and Cr, a mechanism that was also revealed in MD simulations for the latter; in turn it impedes the formation of the 100 loops. The '111 mechanism' also explains the observed dose-rate and temperature effect. However, at low doses (0.05 dpa), it appears that Cr favours the formation of 100 loops, irrespective of the analysis regarding the mobility of the 111 loops. This contradicts the 111 mechanism somewhat, because in this view Cr, reducing the mobility of 111s, should not favour 100 formation. One additional mechanism that might be put forward is a catalytic effect promoting the spontaneous transformation of the 111 loops to 100 loops following Arakawa's suggestions [38]. However, our conclusions indicate that in the case the primary 111 loops are blocked by He there are much less 100 loops, in particular at low dose, which does not support the idea of the spontaneous transformation of 111s to 100s. Besides, there may be a spontaneous transformation to 100 loops of the sessile clusters (including the C15 clusters [11]), which according to MD simulations of displacement cascades in Fe represent a significant fraction of the primary SIA clusters (30–50%) [30]. Moreover, predicting the evolution of the irradiation-induced microstructure by e.g. Monte Carlo numerical simulations is fairly successful only if a good fraction of immobile defects is considered [9], which could be those sessile clusters. Effort should thus now be devoted to the experimental investigation of the sessile clusters in irradiated Fe(Cr).

5. Conclusions

In this study thin foils of UHP Fe and Fe(Cr) alloys were irradiated *in situ* in a TEM via single-beam or dual-beam experiments mainly at room temperature up to a dose of 1 dpa with 500 keV Fe^{+} and 10 keV He^{+} ions to investigate the origin of the self-interstitial atom dislocation loops. The temperature effect was investigated using single-beam irradiation of UHP Fe at liquid nitrogen temperature. The dose-rate effect was investigated at room temperature via single and dual-beam irradiation of UHP Fe. We have tested the idea that 100 loops may stem from the interaction of the mobile 111 loops according to the '111 mechanism'. From our findings we conclude the following:

1. The dose threshold to see defects in Fe(Cr) in TEM is about 10^{-3} dpa, which is before the overlap of displacement cascades. This indicates that dislocation loops can form directly in the collapse of displacement cascades.
2. 111 loops constitute the main primary dislocation loop population in all cases. They can lead to the formation of 100 loops via the 111 mechanism.
3. At 0.5 and 1 dpa in pure Fe the loop population is dominated by 100 loops, which can be explained with the 111 mechanism.
4. In the presence of He the loop population is dominated by 111 loops, indicating that, according to the 111 mechanism, He impedes the movement of 111 loops.

5. At 0.5 and 1 dpa in the presence of Cr there are fewer 100 loops than in pure Fe, indicating that according to the 111 mechanism Cr also impedes 111 loop motion.
6. At 0.05 dpa in pure Fe the microstructure is dominated by 111 loops. This may result from the fact that they have less time to migrate and are less numerous, which frustrates the formation of 100 loops.
7. At 0.05 dpa in the presence of Cr there are more 100 loops than in pure Fe. This indicates that Cr somehow favours the formation of 100 loops, irrespective of its impact on the mobility of 111 loops.
8. Attention should be paid to sessile SIA clusters, including the C15, as they may transform to 100 loops.

Acknowledgments

This work was carried out within the framework of the European Fusion Development Agreement, now EUROfusion, in the MAT-IREMEV project. The Swiss National Science Foundation is thanked for financial support with grants #200020-121877, #200020-140505 and #200021-172934. The authors also acknowledge the outstanding work of the JANNuS Orsay team and ScopeM ETHZ for the overall use of its facility.

References

[1] J.L. Boutard, A. Alamo, R. Lindau, M. Rieth, Fissile core and Tritium-Breeding Blanket: structural materials and their requirements, C. R. Phys. 9 (3-4) (2008) 287–302.
[2] R. Schaublin, J. Henry, Y. Dai, Helium and point defect accumulation: (i) microstructure and mechanical behaviour, C. R. Phys. 9 (3-4) (2008) 389–400.
[3] Y. Serruys, P. Trocellier, S. Miro, E. Bordas, M.O. Ruault, O. Kaitasov, S. Henry, O. Leseigneur, T. Bonnaillie, S. Pellegrino, S. Vaubaillon, D. Uriot, JANNUS: a multi-irradiation platform for experimental validation at the scale of the atomistic modelling, J. Nucl. Mater. 386 (2009) 967–970.
[4] C. Domain, C.S. Becquart, Ab initio calculations of defects in Fe and dilute Fe-Cu alloys, Phys. Rev. B 65 (2) (2002) 024103.
[5] C.C. Fu, F. Willaime, P. Ordejon, Stability and mobility of mono- and di-interstitials in alpha-Fe, Phys. Rev. Lett. 92 (17) (2004) 175503.
[6] G. Wallner, H. Franz, R. Rauch, A. Schmalzbauer, J. Peisl, Diffuse X-ray scattering from defects after low temperature neutron irradiation, Mat. Sci. Forum 15-18 (1987) 907–912.
[7] P. Ehrhart, Investigation of radiation-damage by X-ray-diffraction, J. Nucl. Mater. 216 (1994) 170–198.
[8] F. Willaime, C.C. Fu, M.C. Marinica, J. Dalla Torre, Stability and mobility of self-interstitials and small interstitial clusters in alpha-iron: ab initio and empirical potential calculations, Nucl. Instrum. Methods Phys. Res. Sect. B-Beam Interact. Mater. Atoms 228 (2005) 92–99.
[9] C.C. Fu, J. Dalla Torre, F. Willaime, J.L. Bocquet, A. Barbu, Multiscale modelling of defect kinetics in irradiated iron, Nat. Mater. 4 (1) (2005) 68–74.
[10] D.A. Terentyev, T.P.C. Klaver, P. Olsson, M.C. Marinica, F. Willaime, C. Domain, L. Malerba, Self-trapped interstitial-type defects in iron, Phys. Rev. Lett. 100 (14) (2008) 145503.
[11] M.C. Marinica, F. Willaime, J.P. Crocombette, Irradiation-induced formation of nanocrystallites with C15 laves phase structure in bcc iron, Phys. Rev. Lett. 108 (2) (2012) 025501.
[12] A. Bourret, Irradiation damage in nickel and iron in a high-voltage electron microscope and threshold energy determination, Phys. Status Solidi A-Appl. Res. 4 (3) (1971) 813–825.
[13] S.L. Dudarev, R. Bullough, P.M. Derlet, Effect of the alpha-gamma phase transition on the stability of dislocation loops in bcc iron, Phys. Rev. Lett. 100 (13) (2008) 135503.
[14] B.C. Masters, Dislocation loops in irradiated iron, Nature 200 (490) (1963) 254.
[15] B.C. Masters, Dislocation loops in irradiated iron, Phil. Mag. 11 (113) (1965) 881.
[16] E.A. Little, B.L. Eyre, The geometry of dislocation loops generated in alpha-iron by 1 MeV electron irradiation at 550°C, J. Microsc. 97 (1973) 107–111.
[17] D. Brimbal, B. Decamps, A. Barbu, E. Meslin, J. Henry, Dual-beam irradiation of alpha-iron: heterogeneous bubble formation on dislocation loops, J. Nucl. Mater. 418 (1-3) (2011) 313–315.
[18] D. Brimbal, B. Decamps, J. Henry, E. Meslin, A. Barbu, Single- and dual-beam in situ irradiations of high-purity iron in a transmission electron microscope: effects of heavy ion irradiation and helium injection, Acta Mater. 64 (2014) 391–401.
[19] Z. Yao, M.L. Jenkins, M. Hernandez-Mayoral, M.A. Kirk, The temperature dependence of heavy-ion damage in iron: a microstructural transition at elevated temperatures, Phil. Mag. 90 (35-36) (2010) 4623–4634.
[20] M. Hernandez-Mayoral, Z. Yao, M.L. Jenkins, M.A. Kirk, Heavy-ion irradiations of Fe and Fe-Cr model alloys Part 2: damage evolution in thin-foils at higher doses, Phil. Mag. 88 (21) (2008) 2881–2897.
[21] A.C. Nicol, M.L. Jenkins, M.A. Kirk, Matrix damage in iron, in: G.E. Lucas, L.L. Snead, M.A. Kirk, R.G. Elliman (Eds.), Materials Research Society Symposium - Proceedings, 2001, pp. R1.3.1–R1.3.6.
[22] M.L. Jenkins, C.A. English, B.L. Eyre, Heavy-ion irradiation of alpha-iron, Phil. Mag. A 38 (1) (1978) 97–114.
[23] A. Prokhodtseva, B. Decamps, A. Ramar, R. Schaublin, Impact of He and Cr on defect accumulation in ion-irradiated ultrahigh-purity Fe(Cr) alloys, Acta Mater. 61 (18) (2013) 6958–6971.
[24] A. Prokhodtseva, Modelling Oriented Investigations of Primary Radiation Damage in Ultra High Purity Fe and Fe-cr Alloys (PhD thesis), EPFL, Lausanne, 2013, p. 140.
[25] R. Schaublin, X. Meng, W.M. Stobbs, Weak beam under convergent beam illumination, Ultramicroscopy 83 (3-4) (2000) 145–157.
[26] R.F. Egerton, Electron Energy Loss Spectroscopy in the Electron Microscope, Plenum Press, 1996.
[27] W.W. Wu, R. Schaublin, J.C. Chen, General dislocation image stress of anisotropic cubic thin film, J. Appl. Phys. 112 (9) (2012) 093522.
[28] M.L. Jenkins, Z. Yao, M. Hernandez-Mayoral, M.A. Kirk, Dynamic observations of heavy-ion damage in Fe and Fe-Cr alloys, J. Nucl. Mater. 389 (2) (2009) 197–202.
[29] D.J. Cockayne, Principles and practice of weak-beam method of electron-microscopy, J. Microscopy-Oxford 98 (JUL) (1973) 116–134.
[30] D.J. Bacon, F. Gao, Y.N. Osetsky, The primary damage state in fcc, bcc and hcp metals as seen in molecular dynamics simulations, J. Nucl. Mater. 276 (2000) 1–12.
[31] M.J. Caturla, N. Soneda, E. Alonso, B.D. Wirth, T.D. de la Rubia, J.M. Perlado, Comparative study of radiation damage accumulation in Cu and Fe, J. Nucl. Mater. 276 (2000) 13–21.
[32] N. Soneda, S. Ishino, T.D. de la Rubia, Vacancy loop formation by 'cascade collapse' in alpha-Fe: a molecular dynamics study of 50 keV cascades, Phil. Mag. Lett. 81 (9) (2001) 649–659.
[33] M.J. Aliaga, R. Schaublin, J.F. Loffler, M.J. Caturla, Surface-induced vacancy loops and damage dispersion in irradiated Fe thin films, Acta Mater. 101 (2015) 22–30.
[34] Y.N. Osetsky, A.F. Calder, R.E. Stoller, How do energetic ions damage metallic surfaces? Curr. Opin. Solid St. M 19 (5) (2015) 277–286.
[35] M.R. Gilbert, Z. Yao, M.A. Kirk, M.L. Jenkins, S.L. Dudarev, Vacancy defects in Fe: comparison between simulation and experiment, J. Nucl. Mater. 386-88 (2009) 36–40.
[36] Z. Yao, M. Hernandez-Mayoral, M.L. Jenkins, M.A. Kirk, Heavy-ion irradiations of Fe and Fe-Cr model alloys Part 1: damage evolution in thin-foils at lower doses, Phil. Mag. 88 (21) (2008) 2851–2880.
[37] M.A. Kirk, I.M. Robertson, M.L. Jenkins, C.A. English, T.J. Black, J.S. Vetrano, The collapse of defect cascades to dislocation loops, J. Nucl. Mater. 149 (1) (1987) 21–28.
[38] K. Arakawa, M. Hatanaka, E. Kuramoto, K. Ono, H. Mori, Changes in the burgers vector of perfect dislocation loops without contact with the external dislocations, Phys. Rev. Lett. 96 (12) (2006) 125506.
[39] J. Marian, B.D. Wirth, J.M. Perlado, Mechanism of formation and growth of < 100 > interstitial loops in ferritic materials, Phys. Rev. Lett. 88 (25) (2002) 255507.
[40] H.X. Xu, R.E. Stoller, Y.N. Osetsky, D. Terentyev, Solving the puzzle of < 100 > interstitial loop formation in bcc iron, Phys. Rev. Lett. 110 (26) (2013) 265503.
[41] G. Lucas, R. Schaublin, Helium effects on displacement cascades in alpha-iron, J. Phys. Condens. Mat. 20 (41) (2008) 415206.
[42] J.N. Yu, G. Yu, Z.W. Yao, R. Schaublin, Synergistic effects of PKA and helium on primary damage formation in Fe-0.1%He, J. Nucl. Mater. 367 (2007) 462–467.
[43] K. Morishita, R. Sugano, B.D. Wirth, Thermal stability of helium-vacancy clusters and bubble formation - multiscale modeling approach for fusion materials development, Fusion Sci. Technol. 44 (2) (2003) 441–445.
[44] G. Lucas, R. Schaublin, Stability of helium bubbles in alpha-iron: a molecular dynamics study, J. Nucl. Mater. 386 (2009) 360–362.
[45] D. Terentyev, L. Malerba, A.V. Barashev, On the correlation between self-interstitial cluster diffusivity and irradiation-induced swelling in Fe-Cr alloys, Phil. Mag. Lett. 85 (11) (2005) 587–594.
[46] D. Terentyev, F. Bergner, Y. Osetsky, Cr segregation on dislocation loops enhances hardening in ferritic Fe-Cr alloys, Acta Mater. 61 (5) (2013) 1444–1453.
[47] L.K. Beland, Y.N. Osetsky, R.E. Stoller, H.X. Xu, Interstitial loop transformations in FeCr, J. Alloys Compd. 640 (2015) 219–225.
[48] D. Terentyev, P. Olsson, T.P.C. Klaver, L. Malerba, On the migration and trapping of single self-interstitial atoms in dilute and concentrated Fe-Cr alloys: atomistic study and comparison with resistivity recovery experiments, Comp. Mater. Sci. 43 (4) (2008) 1183–1192.
[49] D. Terentyev, L. Malerba, A.V. Barashev, Modelling the diffusion of self-interstitial atom clusters in Fe-Cr alloys, Phil. Mag. 88 (1) (2008) 21–29.
[50] R.E. Stoller, G.R. Odette, B.D. Wirth, Primary damage formation in bcc iron, J. Nucl. Mater. 251 (1997) 49–60.
[51] D.A. Terentyev, L. Malerba, M. Hou, Dimensionality of interstitial cluster motion in bcc-Fe, Phys. Rev. B 75 (10) (2007) 104108.

[52] D.A. Terentyev, L. Malerba, R. Chakarova, K. Nordlund, P. Olsson, M. Rieth, J. Wallenius, Displacement cascades in Fe-Cr: a molecular dynamics study, J. Nucl. Mater. 349 (1-2) (2006) 119–132.
[53] D. Terentyev, N. Juslin, K. Nordlund, N. Sandberg, Fast three dimensional migration of He clusters in bcc Fe and Fe-Cr alloys, J. Appl. Phys. 105 (10) (2009) 103509.
[54] N. Juslin, K. Nordlund, Molecular dynamics simulations of collision cascades in FeCrHe, Nucl. Instrum. Methods Phys. Res. Sect. B-Beam Interact. Mater. Atoms 267 (20) (2009) 3420–3423.